

Bow shocks, bow waves, and dust waves

William J. Henney & Jorge A. Tarango Yong

Instituto de Radioastronomía y Astrofísica, Universidad Nacional Autónoma de México, Apartado Postal 3-72, 58090 Morelia, Michoacán, México

Accepted XXX. Received YYY; in original form ZZZ

ABSTRACT

Dust waves and bow waves result from the action of a star’s radiation pressure on a stream of dust grains that is flowing past it. They are an alternative mechanism to hydrodynamic bow shocks for explaining the curved arcs of infrared emission seen around some stars. We employ simple cylindrically symmetric models for the dust grain dynamics under the influence of radiation and weak gas–grain coupling, which produce bow shapes that we call dragoids. We also show how thin-shell hydrodynamic models can be modified to treat the case of strong gas–grain coupling, producing bow shapes that we call trapoids. Using our recently developed two-dimensional classification scheme for projected bow shapes, we then analyze the inclination-dependent tracks of the dragoids and trapoids in the planitude–alatitude plane, finding interesting differences from the wilkinoid, cantoid, and ancantoid shapes of hydrodynamic bow shock models. We further show how these are modified in the presence of small-amplitude standing-wave oscillations of the basic shape, as may be produced by hydrodynamic instabilities or a time-varying source. We analyze the prospects of using shape analysis of observational datasets to discriminate between different bow models, finding that sample sizes of order 100 are required.

Key words: circumstellar matter – radiation: dynamics – stars: winds, outflows

1 INTRODUCTION

Curved emission arcs around stars (e.g., Gull & Sofia 1979) are often interpreted as *bow shocks*, due to a supersonic hydrodynamic interaction between the star’s wind and an external stream. This stream may be due to the star’s own motion or to an independent flow, such as an H II region in the champagne phase (Tenorio-Tagle 1979), or another star’s wind (Canto et al. 1996). However, an alternative interpretation in some cases may be a radiation-pressure driven bow wave, as first proposed by van Buren & McCray (1988, §vi). In this scenario, photons emitted by the star are absorbed by dust grains in the incoming stream, with the resultant momentum transfer being sufficient to decelerate and deflect the grains within a certain distance from the star, forming a dust-free, bow-shaped cavity with an enhanced dust density at its edge. Two regimes are possible, depending on the strength of coupling between the gas (or plasma) and the dust. In the strong-coupling regime, gas–grain drag decelerates the gas along with the dust, forming a shocked gas shell in a similar fashion to the wind-driven bow shock case. In the weak-coupling regime, the gas stream is relatively unaffected and the dust temporarily decouples to form a dust-only shell. This second case has recently been studied in detail in the context of the interaction of late O-type stars (which have only weak stellar winds) with dusty photoevaporation flows inside H II regions (Ochsendorf et al. 2014b,a; Ochsendorf & Tielens 2015). We follow the nomenclature proposed by Ochsendorf et al. (2014a), in which *dust wave* refers to the weak coupling case and *bow wave* to the strong coupling case. More complex, hybrid scenarios are also possible, such as that



Figure 1. Bow shocks, bow waves, and dust waves

studied by van Marle et al. (2011), where a hydrodynamic bow shock forms, but the larger dust grains that accompany the stellar wind pass right through the shocked gas shell, and form their own dust wave at a larger radius.

In Tarango Yong & Henney (2018, hereafter Paper I), we proposed a new two-dimensional classification scheme for bow shapes: the projected planitude–alatitude, or Π' – Λ' , diagram. Planitude measures the flatness of the bow’s apex, while alatitude measures the openness of the bow’s wings. Both are dimensionless ratios of lengths that can be estimated from observational images. We have analyzed the inclination-dependent tracks on the Π' – Λ' plane for simple geometric shapes (spheroids, paraboloids, hyperboloids) and for thin-shell hydrodynamic bow shock models (wilkinoid, cantoids,

ancantoids). In this paper, we will do the same for simple models of radiation-driven dust waves (dragoids) and bow waves (trapoids).

The paper is organized as follows. In § 3 we do the same for simple models of a dusty radiation bow wave (dragoids), including the effects of gas-grain drag. In § 4 we investigate the effects on the planitude–alatitude plane of small-amplitude perturbations to the bow shape.

2 DIFFERENT TYPES OF BOW

We will mainly consider the canonical case of a bow around a star of bolometric luminosity, L , with a radiatively driven wind,¹ which is immersed in an external stream of gas and dust with density, ρ , and velocity, v . The size and shape of the bow is determined by a generalized balance of pressure (or, equivalently, momentum) between internal and external sources. We assume that the stream is supersonic and super-alfvenic, so that the external pressure is dominated by the ram pressure: ρv^2 .

2.1 Imperfect coupling between gas and dust

2.2 The case of inside-out bows with external illumination

3 SHAPE OF A DUSTY RADIATIVE BOW WAVE

As an alternative to hydrodynamic or magnetohydrodynamic bow shocks, it is possible that some observed emission arcs may be bow waves due to the action of radiation pressure on dust grains.

A dust grain of geometrical cross-section σ_d situated a distance R from a point source of radiation with luminosity L will experience a repulsive, radially directed radiative force (e.g., Spitzer 1978)

$$f_{\text{rad}} = \frac{\sigma_d Q_p L}{4\pi R^2 c} e^{-\tau} \quad (1)$$

where Q_p is the frequency-averaged² radiation pressure efficiency³ of the grain, c is the speed of light, and τ is the frequency-averaged optical depth between the source and the grain. For simplicity, we will consider only the optically thin case, $\tau \rightarrow 0$.

3.1 Gas-free bow wave

If f_{rad} is the only force experienced by the grain, then it will move on a *ballistic* trajectory, determined by its initial speed at large distance, v_∞ , and its impact parameter, b . For $b = 0$, the grain radially approaches the source with initial radial velocity $-v_\infty$, which is decelerated to zero at the distance of closest approach, R_0 , given by energy conservation:

$$R_0 = \frac{\sigma_d Q_p L}{2\pi c m_d v_\infty^2}, \quad (2)$$

where m_d is the grain mass. The grain then turns round and recedes from the source along the same radius, reaching a velocity of $+v_\infty$

at large distance. For $b > 0$, the trajectory, $R_d(\theta; b)$, is found⁴ to be hyperbolic, characterized by an eccentricity, $\varepsilon = (1 + 4b^2/R_0^2)^{1/2}$, and polar angle of closest approach, $\theta_m = \cos^{-1} \varepsilon^{-1}$. The trajectory is symmetrical about θ_m and can be written as

$$\frac{R_d(\theta; b)}{R_0} = \frac{\frac{1}{2}(\varepsilon^2 - 1)}{\varepsilon \cos(\theta - \theta_m) - 1}, \quad (3)$$

with a total deflection angle of $2\theta_m$, which is equal to 90° when $b = 0.5R_0$.

3.1.1 Parallel dust stream

If the incoming dust grains initially travel along parallel trajectories with varying b , but the same v_∞ , then deflection by the radiative force will form a bow wave around the radiation source, as shown in Figure 5. However, the inner edge of the bow wave, $R_{\text{in}}(\theta)$ is not given by the closest approach along individual trajectories, $R_d(\theta_m; b)$, but instead must be found by minimizing $R_d(\theta; b)$ over all b for each value of θ , which yields

$$\frac{R_{\text{in}}(\theta)}{R_0} = \frac{2}{1 + \cos \theta}. \quad (4)$$

This is the polar form of the equation for the confocal parabola, which we have already discussed in detail in Paper I's § 4 and Appendix A. Its planitude and alatitude are $\Gamma = \Lambda = 2$ and these are unchanged under projection at any inclination.

3.1.2 Divergent dust stream

If the dust grains are assumed to originate from a second point source, located at a distance D from the radiation source, then the incoming stream will be divergent instead of plane parallel. The individual streamlines are not affected by this change and are still described by equation (3), except that the trajectory axes for $b > 0$ are no longer aligned with the global symmetry axis, so we must make the substitution $\theta \rightarrow \theta + \theta_1(b)$, where $\sin \theta_1 = b/D$ (see Fig. 3 of Paper I). We parametrize the degree of divergence as $\mu = R_0/D$ and, as before, $R_d(\theta + \theta_1(b, \mu); b)$ is minimized over all trajectories to find the shape of the bow wave's inner edge. This time, the result is a confocal hyperbola:

$$\frac{R_{\text{in}}(\theta; \mu)}{R_0} = \frac{1 + \varepsilon_\mu}{1 + \varepsilon_\mu \cos \theta}, \quad (5)$$

where the eccentricity is (to first order in μ) $\varepsilon_\mu = (1 - 2\mu)^{-1}$. An example is shown in Figure 5 for $\mu = 0.1$. Unsurprisingly, the resulting bow shape is more open than in the parallel stream case, increasingly so with increasing μ . The planitude and alatitude are both equal: $\Pi = \Lambda = 1 + \varepsilon_\mu$.

3.2 Bow wave with gas drag

More realistically, a grain will also be subject to a drag force, f_{drag} , due to its relative motion with respect to gas or plasma particles. If the gas density, velocity, and sound speed are ρ_{gas} , v_{gas} , and

¹ In § 2.2 we consider the case of an external luminous source.

² Frequency averages of any quantity x should be understood as weighted by the attenuated source spectrum: $\langle x \rangle_\nu = (L e^{-\tau})^{-1} \int_0^\infty x(\nu) L_\nu e^{-\tau_\nu} d\nu$.

³ For absorption efficiency Q_{abs} , scattering efficiency Q_{scat} , and asymmetry parameter (mean scattering cosine) g , we have $Q_p = Q_{\text{abs}} + (1 - g)Q_{\text{scat}}$ (e.g., § 4.5 of Bohren & Huffman 1983).

⁴ The problem is formally identical to that of Rutherford scattering, or (modulo a change of sign) planetary orbits. The method of solution (via introduction of a centrifugal potential term and reduction to a 1-dimensional problem) can be found in any classical mechanics text (e.g., Landau & Lifshitz 1976, § 14).

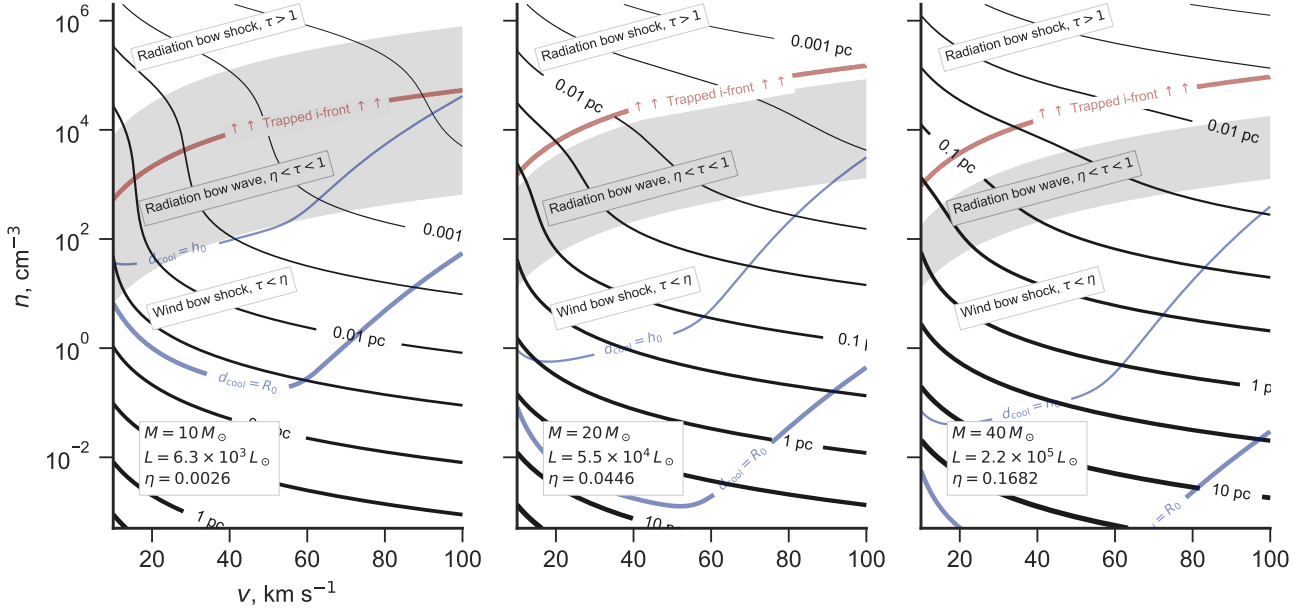


Figure 2. Bow regimes of parameter space (v , n) of the external stream for main-sequence OB stars of different masses: (a) $10 M_{\odot}$, (b) $20 M_{\odot}$, (c) $40 M_{\odot}$.

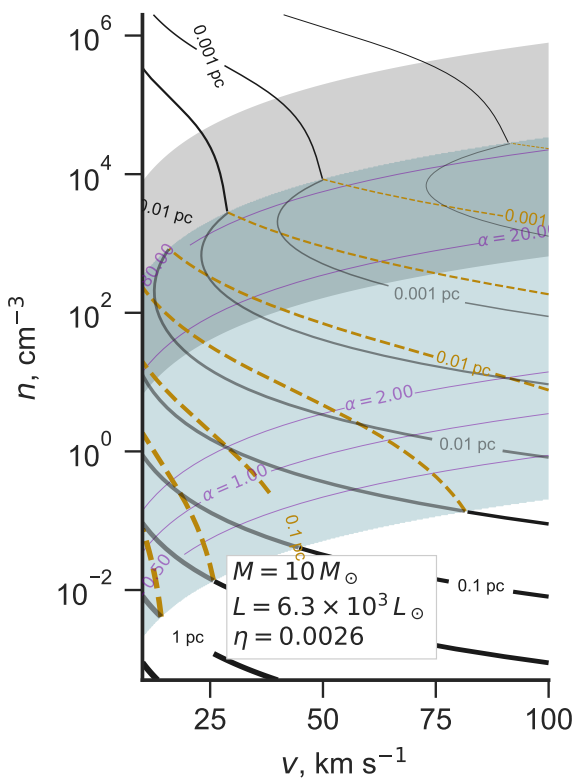


Figure 3. As Fig. 2(a), but accounting for gas-grain decoupling with constant efficiency $\xi = 0.07$.

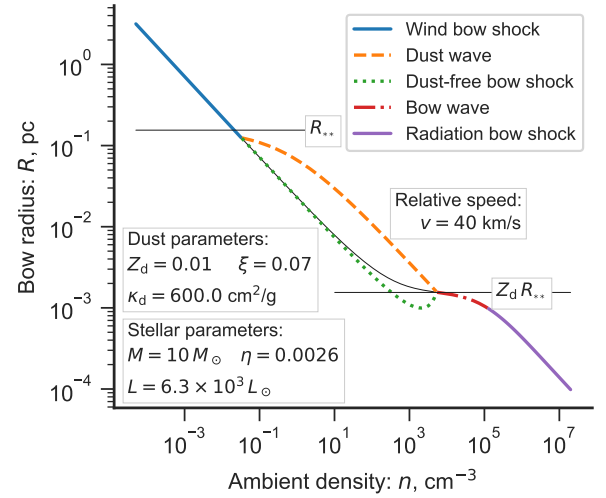


Figure 4. Vertical cut through Fig. 3, showing bow radius and different regimes for a fixed inflow velocity of 40 km s^{-1} .

$c_{s,\text{gas}}$, then a grain with velocity v_d will experience a drag force that is directed opposite to the relative velocity, $\mathbf{w} = \mathbf{v}_d - \mathbf{v}_{\text{gas}}$. In the supersonic limit, $w \equiv |\mathbf{w}| \gg c_{s,\text{gas}}$, the magnitude of the force is

$$|f_{\text{drag}}| \approx Q_{\text{drag}} \sigma_d \rho_{\text{gas}} w^2, \quad (6)$$

where Q_{drag} is an efficiency factor (which may be smaller or greater than unity) that accounts for details such as sticking probability and the boost in cross section when a charged grain interacts with an ionized plasma (Draine & Salpeter 1979). We neglect the back reaction of the dust on the gas motion and

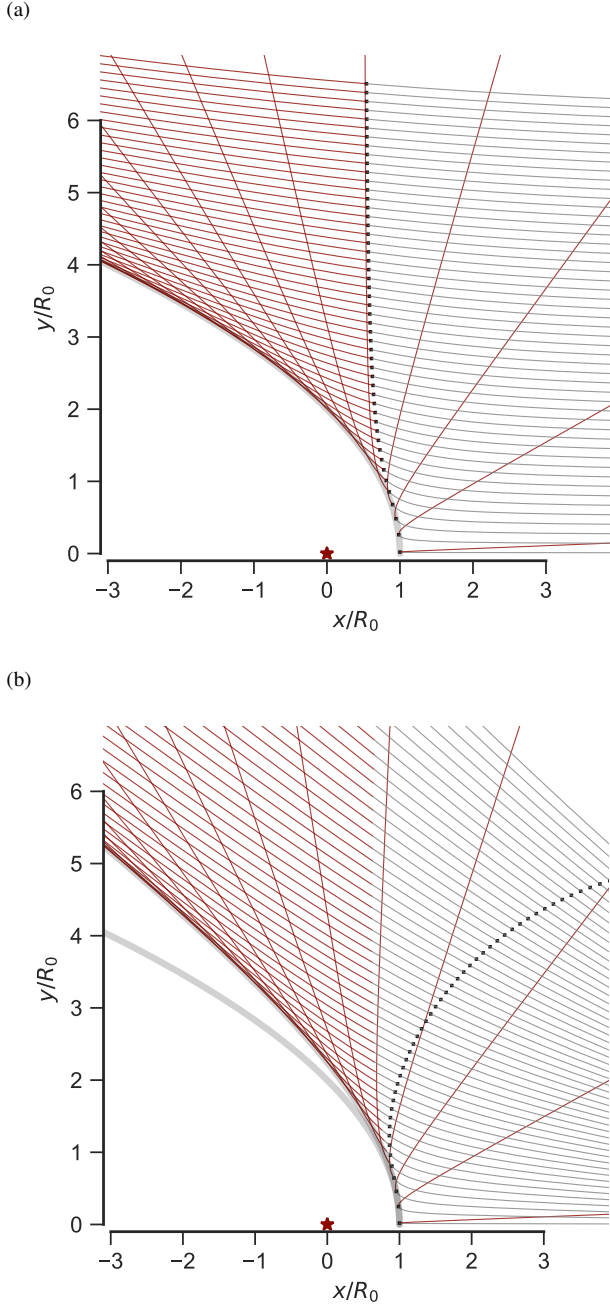


Figure 5. Dust grain trajectories under influence of a repulsive central r^{-2} radiative force. (a) A parallel stream of dust grains approach from the right at a uniform velocity and with a variety of impact parameters (initial y -coordinate). The central source is marked by a red star at the origin, and its radiative force deflects the trajectories into a hyperbolic shape, each of which reaches a minimum radius marked by a small black square. The incoming hyperbolic trajectories are traced in red. The locus of closest approach of the outgoing trajectories is parabolic in shape (traced by the thick, light gray line) and this constitutes the inner edge of the bow wave. (b) The same but for a divergent stream of dust grains that originates from a source on the x axis at a distance $D = 10R_0$ from the origin. In this case, the inner edge of the bow wave is hyperbolic and the parallel stream result is also shown for comparison.

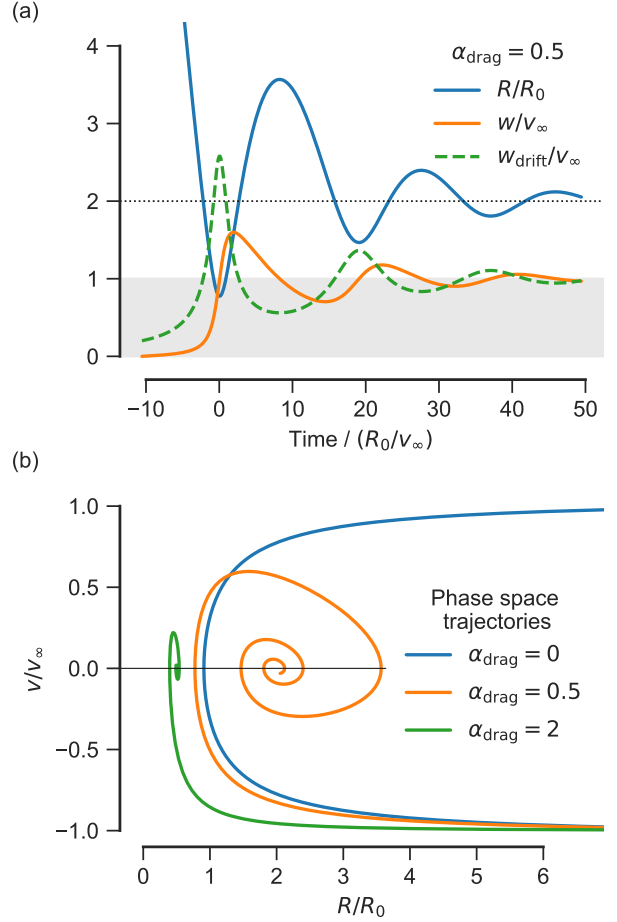


Figure 6. Dust-gas coupling for an on-axis (purely radial) trajectory. (a) Grain radial position, R/R_0 , gas-grain velocity difference, w/v_∞ , and local asymptotic drift velocity, $w_{\text{drift}}/v_\infty$, versus time for $\alpha_{\text{drag}} = 0.5$. The behavior is typical of the dynamics of a damped harmonic oscillator. (b) Phase space (position, velocity) trajectories for $\alpha_{\text{drag}} = 0, 0.5$, and 2 . All trajectories begin in the lower right corner and evolve in a clockwise direction. For $\alpha_{\text{drag}} > 0$, the grain spirals in on the point $(x, u) = (\alpha_{\text{drag}}^{-1}, 0)$.

assume a uniform background gas flow that is perfectly coupled to the incoming dust stream at large radii. So, for the parallel stream case, we have $\mathbf{v}_{\text{gas}} = -v_\infty \hat{\mathbf{x}}$ everywhere.

Considering the incoming flow on the symmetry axis, at each radius there is an asymptotic gas-grain drift speed, w_{drift} , for which the radiative and drag forces exactly cancel, $f_{\text{drag}} = -f_{\text{rad}}$, yielding

$$w_{\text{drift}} = \left(\frac{Q_p L}{4\pi c Q_{\text{drag}} \rho_{\text{gas}} R^2} \right)^{1/2}. \quad (7)$$

Any deviation of w from w_{drift} produces unbalanced forces that tend to restore $w \rightarrow w_{\text{drift}}$, although the grain inertia means that this will not happen instantaneously, so that if w_{drift} varies rapidly along a streamline, then changes in w will lag behind. We define a dimensionless coupling coefficient, α_{drag} , to be the speed of the incoming stream in units of the drift velocity at the radiative turn-around radius:

$$\alpha_{\text{drag}} \equiv \frac{v_\infty}{w_{\text{drift}}(R_0)} = \left(Q_{\text{drag}} \frac{R_0/a_d}{\rho_d/\rho_{\text{gas}}} \right)^{1/2}, \quad (8)$$

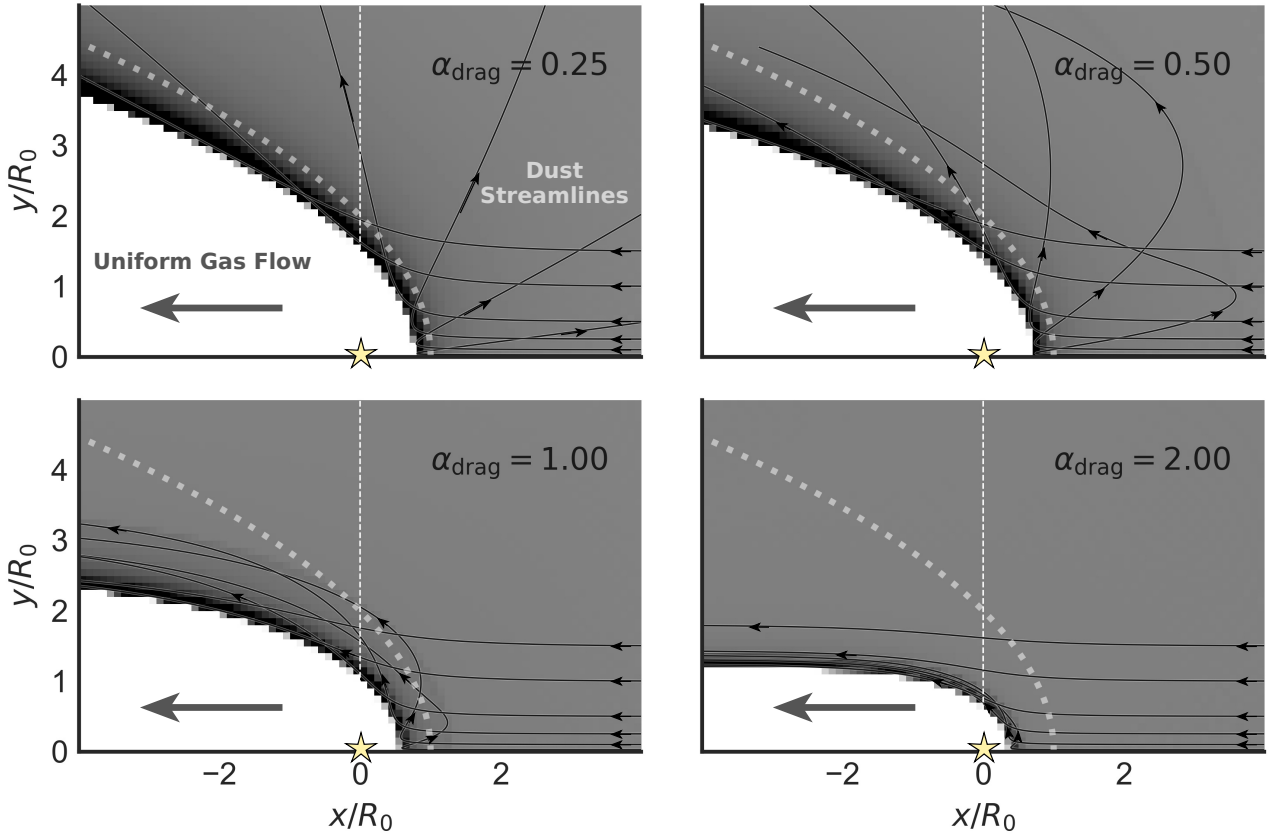


Figure 7. Dust grain trajectories under influence of gas drag in addition to a repulsive central radiative force. The dust streamlines are shown as black lines with arrows and the dust density as a linear gray scale, with maximum (black) of twice the ambient dust density. Results are shown for four values of the drag parameter (see text): $\alpha_{\text{drag}} = 0.25, 0.5, 1.0$, and 2.0 . The shape of the bow wave for the drag-free case (Fig. 5) is shown by the thick dotted line. Faint patterns visible in the density away from the bow wave are numerical aliasing artefacts caused by sparse sampling of the streamlines in the low density regions.

where we have used equation (2) and suppressed a grain-shape dependent geometric factor of order unity. If $\alpha_{\text{drag}} \ll 1$, then $w_{\text{drift}} \gg v_{\infty}$ out to several times the turn-around radius, so the radiation field has no difficulty in effectively decoupling the grain from the gas and producing the velocity difference that is required to turn the grain around and expel it towards the direction whence it came ($w = 2v_{\infty}$). However, for non-zero α_{drag} the R^{-1} dependence of w_{drift} (eq. (7)) means that the grain will *re-couple* to the inflowing gas stream around a radius $\approx R_0/\alpha_{\text{drag}}$ and be swept back in again for another approach to the source. A further effect of increasing α_{drag} is that the grain penetrates closer to the star on its initial approach, thanks to the tail wind provided by the gas flow. Both these behaviors are illustrated in Figure 6, where the inertial lag of w behind w_{drift} means that the phase space trajectory (panel b) is a spiral, which converges on the stagnation point $(R, v) = (R_0/\alpha_{\text{drag}}, 0)$. The cases $\alpha_{\text{drag}} = 0.5$ and $\alpha_{\text{drag}} = 2$ are shown, and it can be seen that with larger α_{drag} the oscillations about the stagnation radius are significantly damped.

However, this description only applies to grains with impact parameter, b , that is exactly zero. Even a very small finite b means that f_{rad} has a component perpendicular to the axis, which pushes the grain to the side and means that, after re-coupling, its second approach is at a much larger impact parameter than its first, so it is dragged around the wings of the bow wave before it can bounce in

and out more than twice. This is illustrated in Figure 7, which shows grain trajectories and the resulting dust density structure, calculated from numerical integration of equations (1) and (6) in 2-D cylindrical coordinates. Results are shown for a range of coupling parameters, α_{drag} . The $\alpha_{\text{drag}} = 0.25$ case appears qualitatively similar to the no-drag case shown in Figure 5a, except that the inner edge of the bow wave has been shifted to a smaller radius. Recoupling of the outgoing streamlines to the gas flow does occur eventually, but on length scales larger than shown in the figure. The $\alpha_{\text{drag}} = 0.5$ case shows the oscillating trajectories discussed above for those grains that come in with a small initial impact parameter. In the $\alpha_{\text{drag}} = 1.0$ case, the oscillating trajectories are more confined, forming a thick shell around R_0 . In the $\alpha_{\text{drag}} = 2.0$ case, the shell is much thinner and concentrated at the inner rim. As α_{drag} increases, the oscillations are damped further so that the stagnation radius R_0/α_{drag} becomes a good approximation to the apex radius of the density wave. All the cases illustrated are for a parallel incident stream, but a divergent stream gives qualitatively similar behavior, as shown in Appendix A. We propose the term *dragoid* for the 3-dimensional shapes of the bow waves, found by rotating results such as Figure 7 about the symmetry axis.

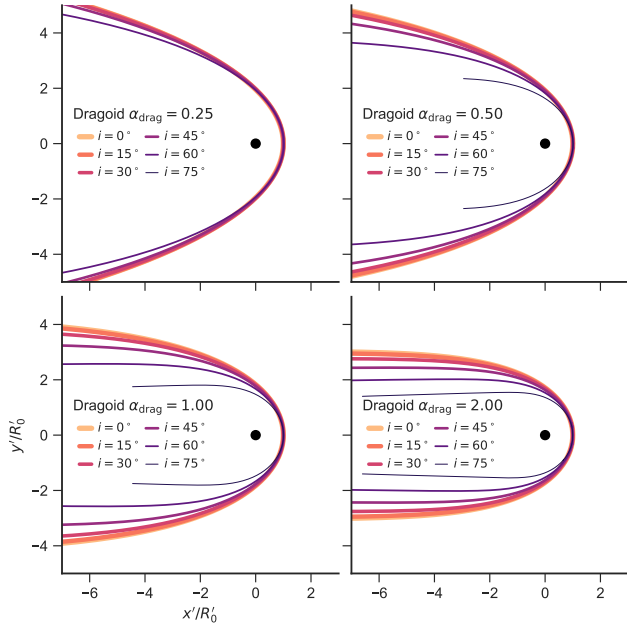


Figure 8. Apparent bow shapes in the plane of the sky for parallel-stream dragoids as a function of inclination angle. Drag coefficient, α_{drag} increases from top-left to bottom-right. Inclination $|i|$ is shown in 15° increments, indicated by line color and thickness (see key).

3.3 Applicability of the bow wave models

The apex turn-around radius, R_0 , of the bow wave depends on the grain properties via the combination $\sigma_d Q_p / m_d$. For grains of size a_d and internal density ρ_d , we have $\sigma_d / m_d \approx (a_d \rho_d)^{-1}$. For radiation with wavelength smaller than the grain size, $\lambda < a_d$, the efficiency is $Q_p \sim 1$, whereas for $\lambda > a_d$ it is $Q_p \sim a_d / \lambda$. Therefore, we would expect R_0 to be almost independent of grain size for small grains, but to vary as $R_0 \propto a_d^{-1}$ for large grains, where small/large is relative to the peak wavelength of the radiation source. In principle, a polydisperse population of grains could produce a blurring of the observed bow wave, but only if large grains contribute significantly to the dust emission.

Variation of α_{drag} with grain size, charged grains.

Lorentz force, Larmor radius

Back-reaction on gas, $\alpha_{\text{drag}} \rightarrow \infty$, recovery of drag-free result for R_0 but with increased effective grain mass.

3.4 Apparent shapes of projected dragoids

4 PERTURBED BOWS

The bow shock models that we have considered so far have been steady-state: although material is moving throughout the bow, the pattern of its structure does not vary with time. In this section, we consider small, time-varying perturbations to such a steady-state structure. These may be due to periodic variations in the momentum-loss rate of one of the winds, or due to dynamical instabilities in the shocked shell.

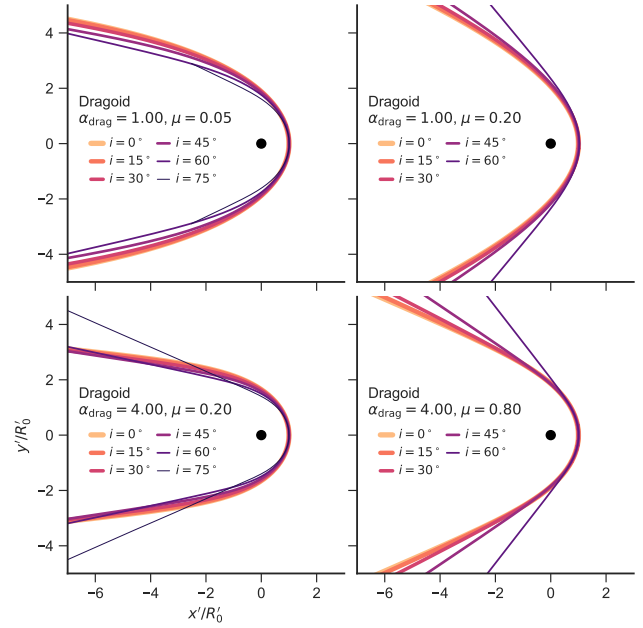


Figure 9. As Fig. 8 but for divergent stream dragoids. Drag coefficient increases from top to bottom, while degree of divergence increases from left to right.

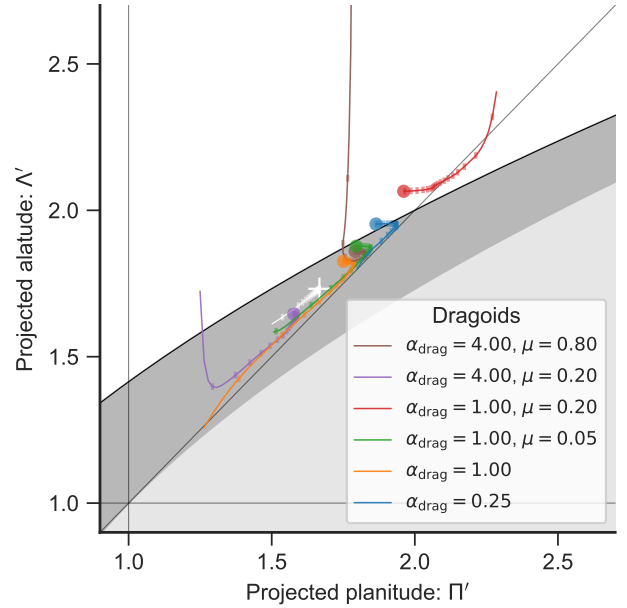


Figure 10. Apparent projected shapes of dragoids in the Π' – Λ' plane. Colored symbols indicate the $|i| = 0$ position for selected models (see key). Thin lines show the inclination-dependent tracks of each model, with tick marks along each track for 20 equal-spaced values of $|\sin i|$. Gray shaded regions are as in Fig. 11a of Paper I. The wilkinooid track is shown in white.

[t!]

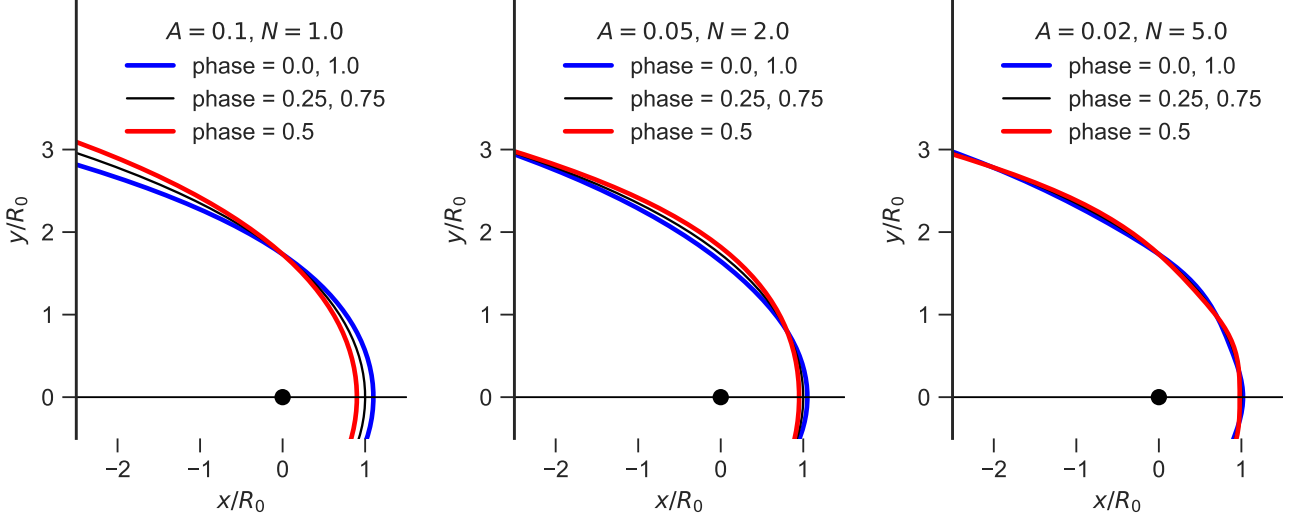


Figure 11. Small-amplitude standing wave perturbations to wilkinoid bow shapes. The maximum deviations from the base shape are seen at phases $\phi = 0$ (blue line) and $\phi = 0.5$ (red line), while the perturbation is zero at $\phi = 0.25$ and 0.75 (black line). Results are shown left to right for increasing wave numbers N and decreasing amplitudes A : (a) $A = 0.1$, $N = 1.0$, (b) $A = 0.05$, $N = 2.0$, (c) $A = 0.02$, $N = 5.0$.

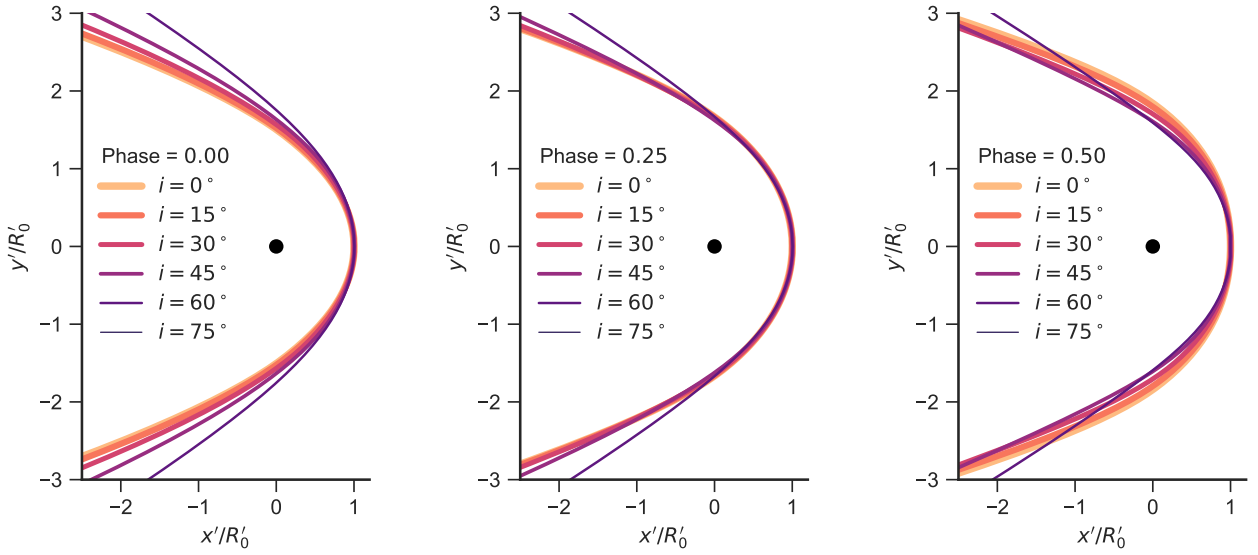


Figure 12. Plane-of-sky projections of perturbed bow shapes. In all cases, the base bow shape is ancantoid with $\xi = 0.8$, $\beta = 0.005$ and the perturbation is the same as in the central panel of Fig. 11, with amplitude $A = 0.05$ and wave number $N = 2.0$. Results are shown for inclination angles $i = 0$ to $i = 75^\circ$ (indicated by line color and thickness, see key) and for different fractional phases of the oscillation: (a) $\phi = 0.0$, (b) $\phi = 0.25$, (c) $\phi = 0.50$. Unlike in Fig. 11, the spatial coordinates are normalized to the instantaneous projected apex radius R'_0 at each phase, so the apex does not appear to move.

We consider fractional perturbations $\Delta(\theta, t)$ of a base shape $R(\theta)$, such that $R(\theta) \rightarrow [1 + \Delta(\theta, t)]R(\theta)$. For simplicity, $\Delta(\theta, t)$ is a standing wave of constant amplitude A , which is periodic in θ , with wave number N . In cylindrical symmetry $\Delta(\theta, t)$ must be even in θ , so can be expressed as

$$\Delta(\theta, t) = A \cos(N\theta) \cos(2\pi\varphi). \quad (9)$$

For waves with period P , the fractional phase φ will vary with time t as

$$\varphi(t) = (\varphi_0 + t/P) \bmod 1.0, \quad (10)$$

where φ_0 is an arbitrary reference phase.

Example oscillations with wave numbers $N = 1.0, 2.0$, and 5.0 superimposed on a wilkinoid base shape are shown in Figure 11. There are N nodes of the oscillation between $\theta = [0, \pi]$, always with an antinode at the apex ($\theta = 0$), as required by symmetry. So, with $N = 1.0$ there is a node (fixed point) in the near wing at $\theta = \pi/2$, but an antinode in the far wing at $\theta = \pi$, which is in antiphase with the oscillation of the apex, giving rise to a large-scale “breathing” mode of oscillation. With $N = 2.0$, there are nodes at $\theta = \pi/4$ and $3\pi/4$, while the antiphase antinode has moved to the near wing at $\theta = \pi/2$. There is still an antinode in the far wing at $\theta = \pi$ but it is now in phase with the apex, giving rise to a “curling-up/straightening-out” mode of oscillation. With $N = 5.0$, there are many more nodes and antinodes, giving a “ringing” mode of oscillation. Note that all our examples have $A \propto 1/N$ in order to keep the local curvature relatively low. If the product AN is not small compared to unity, then the local curvature can be so extreme as to reverse the concave shape of the base bow shape, producing locally convex regions.

If the bow shape is viewed at different inclinations, then the effect of the oscillations on the projected shape will vary. In particular, the apex-to-wing interval in body-frame angle changes from $\theta = [0, \pi/2]$ at $i = 0$ to $\theta = [\theta_0, \theta_{90}]$ for general i , see equations (18) and (21) of Paper I. The difference $\theta_{90} - \theta_0$ is always a declining function of $|i|$, so the oscillations of the tangent line become increasingly stretched out as the inclination increases. This effect can be seen in Figure 12, which shows an example of the variation in projected perturbed shape with inclination angle for 3 different phases, this time for an ancantoid base shape and the $N = 2.0$ perturbation shown in Figure 11b. The most marked changes with phase are seen for low inclinations, whereas the changes are smaller, although still noticeable, for $|i| \geq 45^\circ$. If AN exceeds about 0.5, then the local curvature of the perturbations is so extreme that multiple tangent lines exist at intermediate inclinations, which produces the appearance of additional incomplete bright arcs inside the main arc of the bow.

5 SUMMARY AND DISCUSSION

How different regions of the Π – Λ plane are populated. Bottom-right quadrant hard to get to (except for standing wave oscillations), but may be due to finite shell thickness, which (for low Mach number) will be more apparent in the wings, which might decrease Λ more than Π . Fact that thin-shell solutions should trace the contact discontinuity, but in some cases it may be only the inner or the outer shell that is visible.

Justification for standing waves: Fig. 3 of Meyer et al. (2016) shows a time sequence of thin-shell instability, which looks a bit like a standing wave. But much larger amplitude than we are considering.

Deviations from axisymmetry as an alternative to oscillations.

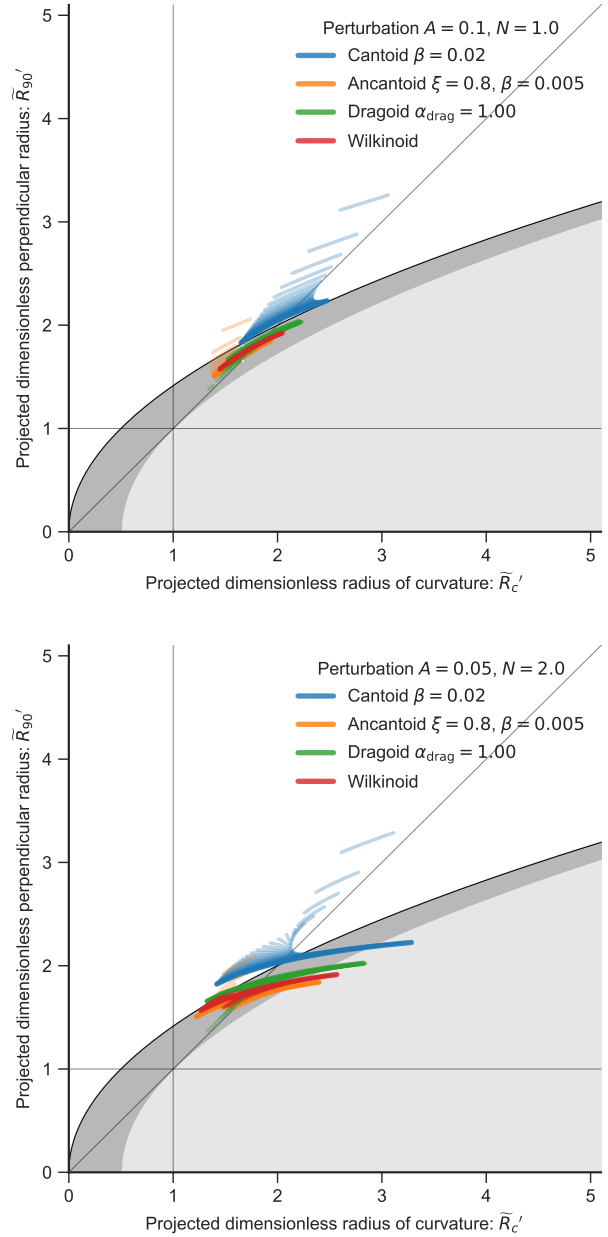


Figure 13. Diagnostic diagram for perturbed shapes

REFERENCES

- Bohren C. F., Huffman D., 1983, Absorption and scattering of light by small particles. Wiley-VCH
- Canto J., Raga A. C., Wilkin F. P., 1996, *ApJ*, **469**, 729
- Draine B. T., Salpeter E. E., 1979, *ApJ*, **231**, 77
- Gull T. R., Sofia S., 1979, *ApJ*, **230**, 782
- Hindmarsh A. C., 1983, *IMACS Transactions on Scientific Computation*, **1**, 55
- Jones E., Oliphant T., Peterson P., et al., 2001–2017, SciPy: Open source scientific tools for Python, <http://www.scipy.org/>
- Landau L., Lifshitz E., 1976, *Mechanics*, 3rd edn. Course of Theoretical Physics S Vol. 1, Butterworth-Heinemann
- Meyer D. M.-A., van Marle A.-J., Kuiper R., Kley W., 2016, *MNRAS*, **459**, 1146

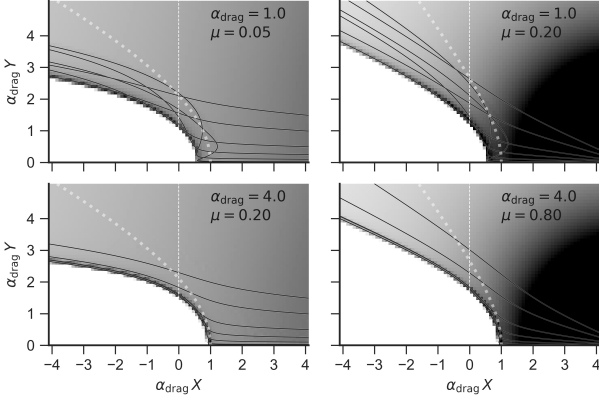


Figure A1. Divergent dragoids

Ochsendorf B. B., Tielens A. G. G. M., 2015, *A&A*, 576, A2
 Ochsendorf B. B., Cox N. L. J., Krijt S., Salgado F., Berné O., Bernard J. P., Kaper L., Tielens A. G. G. M., 2014a, *A&A*, 563, A65
 Ochsendorf B. B., Verdolini S., Cox N. L. J., Berné O., Kaper L., Tielens A. G. G. M., 2014b, *A&A*, 566, A75
 Spitzer L., 1978, *Physical processes in the interstellar medium*. New York: Wiley-Interscience
 Tarango Yong J. A., Henney W. J., 2018, *MNRAS*, in preparation
 Tenorio-Tagle G., 1979, *A&A*, 71, 59
 van Buren D., McCray R., 1988, *ApJ*, 329, L93
 van Marle A. J., Meliani Z., Keppens R., Decin L., 2011, *ApJ*, 734, L26

APPENDIX A: EQUATIONS OF MOTION FOR GRAINS WITH RADIATION AND GAS DRAG

To find the dust grain trajectories $R_d(\theta)$ in the presence of radiation and drag forces (§ 3.2), we numerically integrate the equations of motion. We define dimensionless cylindrical polar coordinates,

$$(X, Y) = \left(\frac{R_d(\theta) \cos \theta}{R_0}, \frac{R_d(\theta) \sin \theta}{R_0} \right), \quad (\text{A1})$$

and dust grain velocities,

$$(U, V) = \left(\frac{\mathbf{v}_d \cdot \hat{\mathbf{x}}}{v_\infty}, \frac{\mathbf{v}_d \cdot \hat{\mathbf{y}}}{v_\infty} \right), \quad (\text{A2})$$

where $\hat{\mathbf{x}}$ and $\hat{\mathbf{y}}$ are unit vectors along the X and Y axes (parallel and perpendicular, respectively, to the symmetry axis). The grain equation of motion then follows from equations (1, 2, 6–8) as the following set of coupled differential equations:

$$\begin{aligned} \frac{dX}{dt} &= U & \frac{dY}{dt} &= V \\ \frac{dU}{dt} &= \frac{1}{2} \left[X (X^2 + Y^2)^{-3/2} - \alpha_{\text{drag}}^2 D_1 (U - U_1) \right] \\ \frac{dV}{dt} &= \frac{1}{2} \left[Y (X^2 + Y^2)^{-3/2} - \alpha_{\text{drag}}^2 D_1 (V - V_1) \right], \end{aligned} \quad (\text{A3})$$

where (U_1, V_1) are the components of the gas velocity (assumed fixed), given by

$$(U_1, V_1) = \begin{cases} \text{parallel stream} & (-1, 0) \\ \text{divergent stream} & \left(\frac{X - \mu^{-1}}{R_1}, \frac{Y}{R_1} \right), \end{cases} \quad (\text{A4})$$

where

$$R_1 = \left((X - \mu^{-1})^2 + Y^2 \right)^{1/2} \quad (\text{A5})$$

is the distance from the second source, located at $(X, Y) = (\mu^{-1}, 0)$. The dimensionless gas density, D_1 , normalized by the value at $(X, Y) = (1, 0)$, is

$$D_1 = \begin{cases} \text{parallel stream} & 1 \\ \text{divergent stream} & \frac{(\mu^{-1} - 1)^2}{R_1^2}. \end{cases} \quad (\text{A6})$$

Equations (A3) are integrated using the python wrapper `scipy.integrate.odeint` to the Fortran ODEPACK library (Hindmarsh 1983; Jones et al. 2017), with results shown in Figure 7 for parallel-stream cases and Figure A1 for divergent-stream cases.

This paper has been typeset from a \LaTeX file prepared by the author.